Energy absorption study of warm-rolled dual-phase LZ71 magnesium alloy hollow tube using ANN

Mostafa Pahlavani[1], Javad Marzbanrad[1*]

[1] School of Automotive Engineering, Iran University of Science and Technology, Tehran, Iran.

ARTICLE INFO	ABSTRACT
	In the present work, the energy absorption study of warm-rolled LZ71 sheet is done for the first time. To do so, Lithium (7% Wt), Zinc (1% Wt) and Magnesium are cast in 770^0 C. After that, the billet has been warm-rolled at 350^0 C and its thickness reduced by 80%. Then, two different heat treatment situations are studied to reach an isotropic plate. Afterward, microstructures of the specimens have been studied using an optical microscope. Tensile tests of the samples are derived to study the mechanical and anisotropy properties of the sheets. Moreover, the results of tensile tests applied for crushing simulations. Energy absorption study of the alloy is also done using ABAQUS software. The results of simulations are validated using experimental tests of AA6082 and completely acceptable performance of simulations is observed. Then, the mechanical properties of LZ71 are used to study the crashworthiness behavior of the mentioned alloy. Crash absorption parameters, namely peak crushing force (F_{Max}), mean crushing force (F_{Mean}), Total Energy Absorption (TAE), Crushing Force Efficiency (CFE), Specific Energy Absorption (SEA) and Total Efficiency (TE) of LZ71 and AA6082 are compared which shown that the performance of LZ71 is considerably more efficient than that of AA6082. Lastly, by the help of Artificial Neural Network (ANN) and Taguchi Method, the effects of dimensional parameters of tube, namely diameter, length and thickness, on F_{Max}, F_{Mean}, TAE, CFE, SEA and TE are surveyed comprehensively.

1. Introduction

Recently, many researchers are concentrated on control of collision kinetic energy [1-5]. Generally, there are various applications of energy absorption such as civil engineering [6], vehicle design [7-9], aerospace engineering [10, 11], etc. Basically, energy absorber converts kinetic energy into some other form of energy. Approximately, principles of all kinds of structural energy absorbers performance are based on its collapse. In the field of automotive engineering, because of the effective role on the safety of passenger cars, research on crash energy absorbers is considerably important [12]. Vehicle crash boxes are the most common structural energy absorbers which are used in various shape, namely cylindrical, tapered, polygonal etc. [13-16]

There are various experimental, analytical and simulation surveys on thin-walled structures energy absorption in several categories such as collapsing [17-19], flattening [20, 21], inversion [22, 23], bending [24-26], rupture [27-30], etc. Each mechanism has some special characteristics and also has specific applications.

Alavi Nia and Khodabakhsh [31] worked on concentric thin-walled tubes energy absorption. Their study includes simulations and experiments

*Corresponding Author
Email Address: marzban@iust.ac.ir

of quasi-static and dynamic loading. They conclude that comparing concentric tubes and a single tube system with an equal mass of structures absorbed the energy of the two-tube system is more than the single-tube system.

Tubular structures have considerable importance in the field of crashworthiness, due to its effect on occupant injury reduction in a crash [32]. Low cost, high strength and stiffness, excellent load efficiency and energy absorption capacity are the main reasons to make tubular crash absorbers pervasive applicable in engineering. [33]. Hence, it seems to be obligatory to study on crushing behavior aiming to increase the energy absorbing capability of tubular structures [34]. Marzbanrad and Ebrahimi [12] used the explicit finite element method to simulate the crushing behavior of tubular energy absorber. They presented a method using the genetic algorithm (GA) and artificial neural network (ANN) to determine the best geometrical conditions of crash absorber based on optimizing the CFE and SEA of the structure.

Meanwhile, the geometry of crash absorbers has been the subject of various researches [35]. For instance, tapered crash absorbers have been considered due to their absorption performances [36]. Hou et al. [37] had a numerical study on tapered circular tubes. They used Multi Objective Optimization (MOO) and Design of Experiment (DoE) to achieve an optimized geometry of hollow single, foam-field single and collinear double tubes tapered crash absorber. Taştan et al. [38] researched on the crashworthiness of tapered thin-walled tubes with lateral circular cutouts. In their work, the performance of tapered crash absorbers including lateral circular cutouts has been surveyed numerically. Crush Force Efficiency (CFE) and the Specific Energy Absorption (SEA) have been considered as the main parameters of the absorbers crashworthiness performance, which computed using the finite element analysis.

Study on the effects of different types of metal forming and work hardening on mechanical properties and formability of materials in interesting for researchers [39-42]. The constituent material of the crash absorbers is also an interesting area which attracted numerous researchers [43-46]. In addition, magnesium alloys applications are experiencing a sharp rise in various industries such as Automotive, Aerospace, and Electronics due to its proper mechanical behavior [46-49]. Moreover, these alloys are well known as the lightest structural alloys having considered the density of 1.8 gr/cm3 or even less [50, 51]. Pure magnesium is one of the most abundant metals and has considerable properties, namely high durability,

very high strength to weight ratio, high recyclability, desirable heat loss and electromagnetic shielding [52, 53]. Magnesium-Lithium alloys are one of the most favorable engineering metal due to its incredible properties, such as high formability and ultralow density [48]. Kiani et al. [54] had research on the design of lightweight magnesium vehicle structure. They used Dodge Neon impact data to compare their simulation performance. Some steel structural components have been replaced by AZ31 magnesium alloy to study crashworthiness effects of this lightweight alloy.

Mg-Li alloys are obviously attractive due to its elongation beside the distinct low density [55]. To achieve more proper mechanical properties, adding rare earth elements to the compound will be an effective solution. However, Mg-Li alloys containing 5 to 12 lithium weight proportion have the best structural behavior due to the fact that this portion of lithium will cause dual phase microstructure of the alloy with α-Mg (Mg solid solution, hcp structure) and β-Li (Li solid solution, body centered cubic (bcc) structure) [56].

In the present study, mechanical properties of LZ71 magnesium alloy are carried out and crashworthiness characterizations of LZ71 are studied numerically. Also, the Taguchi method is used to identify the dimensional parameters of the tubes to reduce simulation number. Moreover, crashworthiness sensitivity of LZ71 hollow tube regarding dimensional parameters is observed using the Artificial Neural Network (ANN).

2. Experimental Procedure

2.1. Alloy Preparation

In the present study, LZ71 alloy (Mg-7(Wt%) Li-1(Wt%) Zn) is cast using high-frequency Induction furnace at almost 770^0 C under argon protective atmosphere. Then the melt was cast into a preheated steel mold (Figure 1:). The initial ingot has been warm-rolled from initial thickness of 10mm to final thickness of 2mm (total reduction of around 80% in 8 passes by 10% reduction) at a rolling temperature of 350°C (Figure 2:). The sheet was then annealed at 200^0 C and 350^0 C for 3 hours.

Figure 1: As cast ingots.

Figure 2: Warm rolled sheet.

2.2. Metallography

To study the microstructure of the prepared alloy HUVITS HR3-TRF-P Optical Microscope (OM) is used. The specimens were ground, polished and corroded in the etchant solution of water (150 ml), HNO_3 (1 ml), CH_3COOH (1 ml) and $H_2C_2O_4$ (1 gr). Then, specimens were rinsed by alcohol and dried. After this, the micrographs of specimens have been taken on image analyzer and optical microscope.

2.3. Mechanical Properties

Mechanical properties of as-cast Mg LZ71, as rolled and full annealed are studied by uniaxial tensile tests. The test samples were prepared oriented along the rolling direction according to the ASTM E08 standard. Figure 3:.a shows the tensile tests specimens which are cut in three directions, namely rolling direction (RD), 45^0 and transverse direction (TD) as illustrated in Figure 3:.b. Uniaxial tensile tests were done at an initial strain rate of 1 mm/min at room temperature using SANTAM STM-50 tensile testing machine.
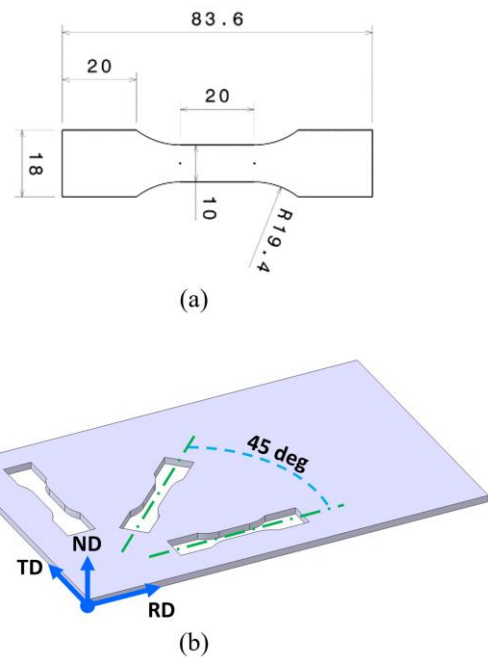

Figure 3: Tensile tests specimens: a) Dimensions, b) Cutting directions.

3. Energy absorption

3.1. Design parameters

Plastic deformability of an energy absorber before the fracture is known as its crashworthiness capability. There are several criteria to determine the crashworthiness capacity of crash absorbers, which are based on the force-displacement curve [57]. The most common crashworthiness criteria are described below.

1) Total energy absorption (TEA): defined as external work of the tube which can be calculated as:

$$TEA = \int F(\delta)d\delta = \sum_{i=2}^{N-1} F_i \times \left(\frac{\delta_{i+1} - \delta_{i-1}}{2}\right) \quad (1)$$

where F(δ) is a function of the crash load based on the tube deformation (δ). Indeed, TEA could be considered as the area under the force-displacement diagram.

2) Peak crush force (F_{Max}): the maximum axial force on the part.

3) Mean crush force (F_{Mean}): the result of division of TEA to total crush displacement (δ_t).

$$F_{mean} = \sum_{i=2}^{N-1} \frac{P_i \times \left(\frac{\delta_{i+1} - \delta_{i-1}}{2}\right)}{\delta_t} \qquad (2)$$

4) Crush force efficiency (CFE): the result of division of mean crush force to peak crush force:

$$CFE = \frac{F_{Mean}}{F_{Max}} \qquad (3)$$

5) Specific energy absorption (SEA): the ratio of total absorbed energy to part mass:

$$SEA = \frac{TEA}{m} \qquad (4)$$

where m is the tube mass which absorbs energy during impact.

6) Total Efficiency (TE): the ratio of total absorbed energy to the products of F_{max} and total length of structure:

$$TE = \frac{F_{Mean} \times \delta}{F_{Max} \times L} \qquad (5)$$

3.2. Finite Element Modelling

In the present study, the commercially available explicit dynamic nonlinear FE analysis code ABAQUS/Explicit software has been used to carry out the crush numerical simulations. Also, commercial mesh generation software HYPERMESH is used to mesh the models. Four-node shell elements with reduced integration are selected to simulate the circular tube crashes. The crash simulation model is shown in Figure 4: which is included the bottom and top rigid walls and circular tube as a crash absorber. Quasi-static simulation is performed to study the crashworthiness of the structure. Also, friction coefficients between tubes and rigid walls have been considered 0.2. To investigate mesh convergence, various element sizes were studied to discretize the circular structure. The effect of mesh size on mean crush force and total energy absorption is observed to study the accuracy of the model. This should be noticed, crash energy absorption parameters are calculated for the first 70% of tube length.
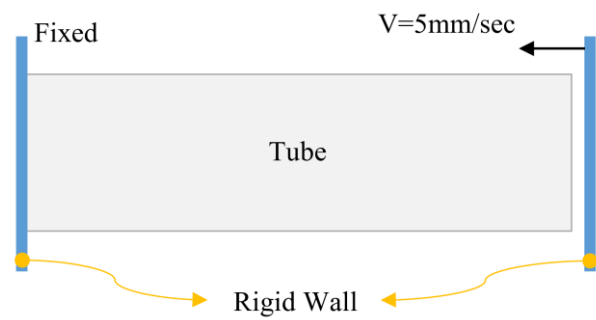

Figure 4: Crash model schematic.

Figure 5: and Table 1: present F_{Mean} and F_{Max} from the FE models of two circular tubes (A1 and A4) regarding element size 1.5 to 5 mm. Length, thickness and the outer diameter of the A1 model are 101.6, 1.6 and 50.8 respectively and also the mentioned geometrical parameters of the A4 model are 152.4, 1.6, and 76.2 respectively. Dimensions and samples names are similar to [58] which its experimental results are used in the present work. It could be seen that the convergence has been attained at the element size of 2 mm.
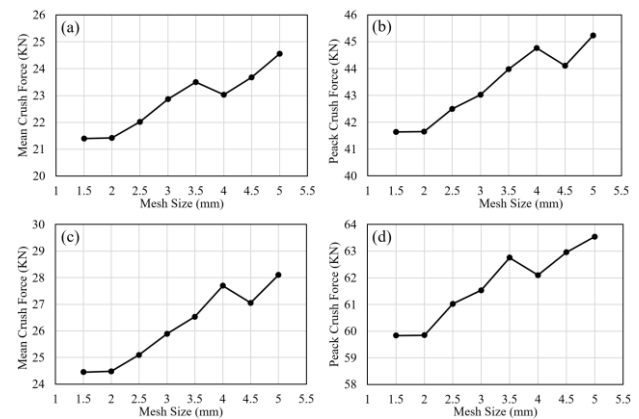

Figure 5: F_{Mean} and F_{Max} against mesh size: (a) and (b) A1 model, (c) and (d) A4 model.

Table 1: Convergence of mean crush force versus mesh size

Mesh Size (mm)	Number of Elements		F_{Mean} (KN)		F_{Max} (KN)	
	A1	A4	A1	A4	A1	A4
5	648	1458	24.561	28.101	45.234	63.543
4.5	800	1801	23.672	27.056	44.103	62.957
4	1013	2279	23.028	27.698	44.762	62.102
3.5	1323	2977	23.495	26.534	43.985	62.756
3	1801	4052	22.863	25.895	43.026	61.536
2.5	2593	5834	22.019	25.102	42.503	61.023
2	4052	9116	21.45	24.143	41.651	59.849
1.5	7203	16206	21.399	24.11	41.643	59.838

3.3. Validation of the FEA

To validate the FE simulations, in the present study, the results presented by Lu [58] have been used. Energy absorption parameters of the simulations of the present study, having considered Aluminum AA6082 tubes mechanical properties, as compared to the experimental results carried out by Lu [58]. Figure 6: shows the stress-strain curve of annealed Aluminum AA6082.
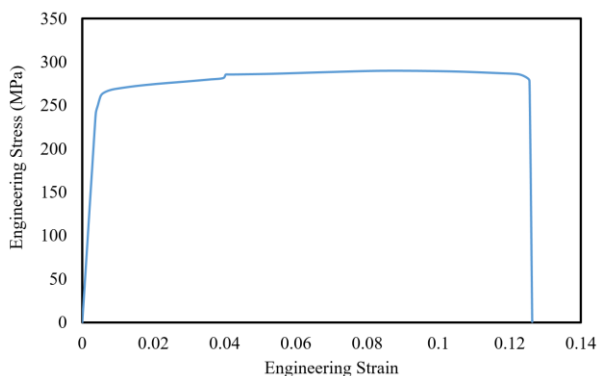
Figure 6: Stress-Strain curve of annealed Aluminum AA6082. [58]

To compare the accuracy of the FE simulation of the present work comprehensively, six experimental sample data, namely A1, A2, A4, A5 and A7 (as were called in [58]) are selected to compare with the FE simulations results.

Dimensions of the mentioned samples are presented in Table 2:, where L, t, D, and M are length, thickness, outside diameter and mass of the specimens respectively. Comparison of crush modes and force-displacement curve are illustrated in Figure 7: and Figure 8: respectively.

As can be seen from Figure 7:, A1, A2, and A7 FE simulation samples are collapsed exactly similar to experimental ones (Figure 7:. a, b, and e). A4 FE simulation sample is collapsed in symmetrical mode while A4 experimental sample experienced a fold in the bottom of the tube separated from other folds (Figure 7:. c).

In addition to collapse mode shape, the simulations force-displacement graphs showed a close agreement compared with the experimental data properly, as illustrated in Figure 8:. In all simulated models, F_{Max} are more than experiments and the first fold peak force is overall peak force (F_{Max}).

**Table 2:** Dimensions and mass of A1, A2, A4, A5, and A7 samples.

Specimen No.	L (mm)	t (mm)	D (mm)	D/t	L/D	M (Kg)	
						AA6082	LZ71
A1	101.6	1.6	50.8	31.75	2	0.07	0.0394
A2	101.6	3.25	50.8	15.63	2	0.14	0.0788
A4	152.4	1.6	76.2	47.63	2	0.16	0.0901
A5	152.4	3.25	76.2	23.45	2	0.32	0.180
A7	203.2	1.6	101.6	63.5	2	0.28	0.158

Also, the parameters of crash absorption of experiments and simulations are compared in Table 3:. The maximum difference of F_{mean} is regard to A1 sample by -4.684% and overall absolute division of all samples is 2.97%. Maximum and average absolute deviations of F_{max} between experiments and simulations are 9.846% and 3.859% respectively. Maximum differences of TEA, CFE, and SEA are -4.684%, -6.515% and -4.684%, respectively, while overall absolute divisions of the mentioned parameters between simulations and experiments are 2.907%, 4.288%, and 2.907%, respectively. As can be seen, maximum and average of differences are less than 10% for each case and parameter, which depict proper simulations results.
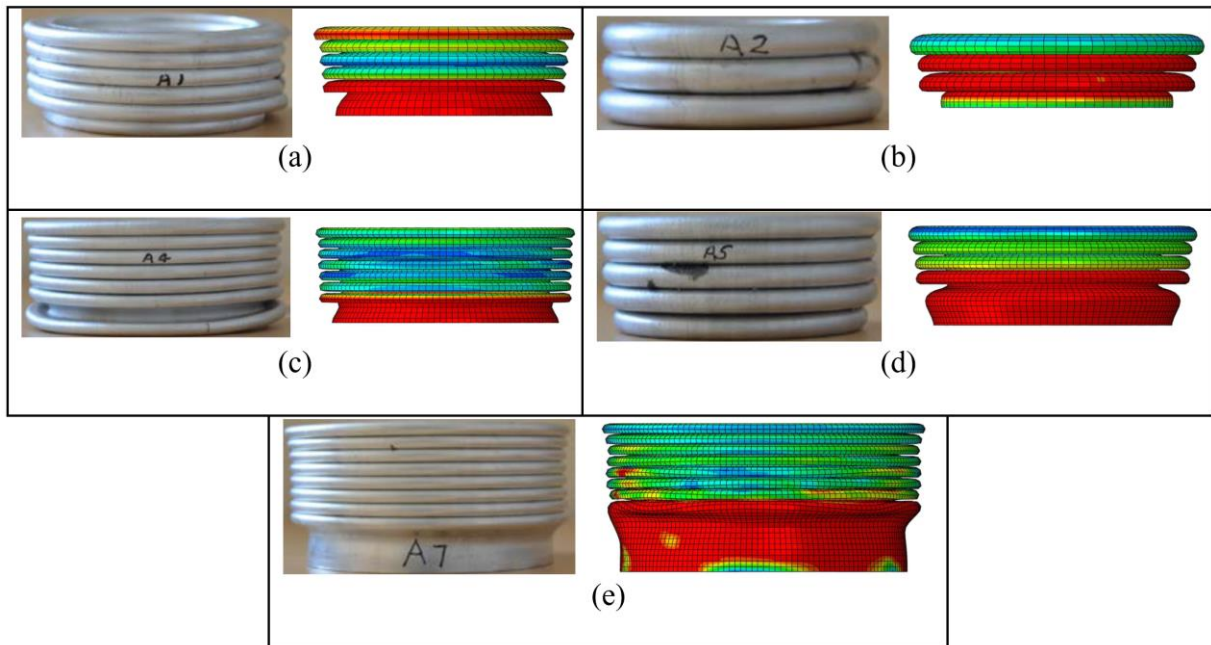
Figure 7: Crush mode comparison of experiments [58] versus simulations: a) A1, b) A2, c) A4, d) A5, e) A7.
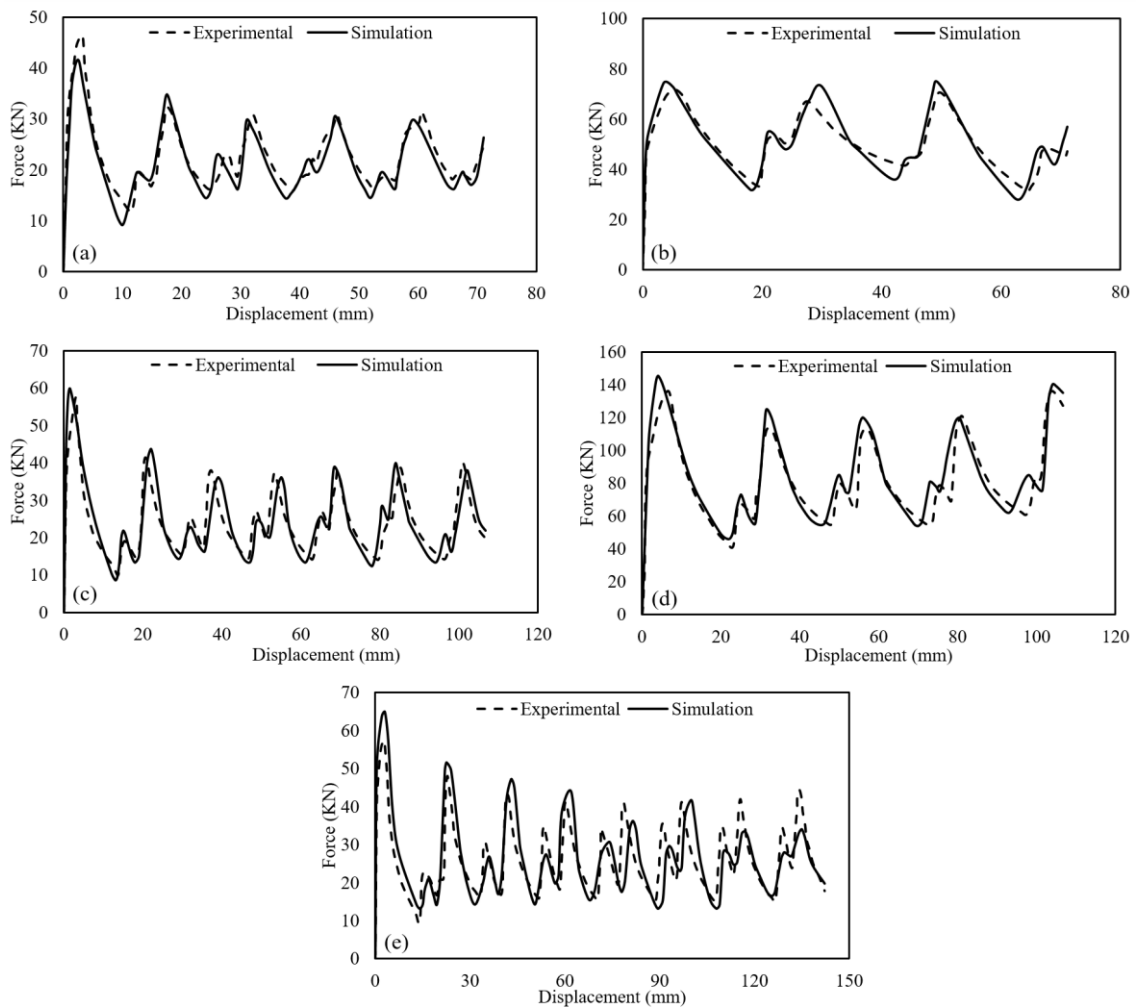
Figure 8: Force-Displacement results of experiments [58] versus simulations: a) A1, b) A2, c) A4, d) A5, e) A7.

Energy absorption study of warm-rolled dual-phase LZ71 magnesium alloy hollow tube using ANN

Table 3: Comparison of energy absorption parameters of experiments [58] versus simulations for 5 samples.

	Specimen No.	A1	A2	A4	A5	A7
F_{mean}	Experiments (KN)	22.504	50.476	23.841	81.330	26.122
	FE Simulations (KN)	21.450	49.008	24.149	84.310	26.725
	Differences (%)	-4.684	-2.907	1.295	3.664	2.307
F_{max}	Experiments (KN)	46.200	71.600	57.500	135.900	57.700
	FE Simulations (KN)	41.651	74.363	59.849	145.358	61.132
	Differences (%)	-9.846	3.859	4.085	6.960	5.948
TEA	Experiments (KJ)	1600.466	3589.821	2543.324	8676.280	3715.595
	FE Simulations (KJ)	1525.499	3485.458	2576.267	8994.202	3801.328
	Differences (%)	-4.684	-2.907	1.295	3.664	2.307
CFE	Experiments	0.487	0.705	0.415	0.598	0.453
	FE Simulations	0.515	0.659	0.404	0.580	0.437
	Differences (%)	5.726	-6.515	-2.680	-3.081	-3.436
SEA	Experiments (KJ/Kg)	22863.795	25641.577	15895.775	27113.376	13269.984
	FE Simulations (KJ/Kg)	21792.846	24896.129	16101.669	28106.880	13576.171
	Differences (%)	-4.684	-2.907	1.295	3.664	2.307

3.4. Sensitivity of Crash Absorption Parameters to Dimensions

3.4.1. Model Fitness

To study the trends of crash absorption parameters versus diameter, length and thickness, the Taguchi method is applied to determine the geometry of tubes which are needed. Taguchi method is introduced by Taguchi and Konishi, has been vastly utilized in engineering to optimize performance, quality, cost etc. according to the design parameters [59]. This method is known as one of the most important tools for a powerful and robust design of experiments [60]. In the present study, Diameter, Thickness, and Length of the tube are considered as design parameters which are set in 5 levels as can be seen in Table 4:. The main reason for using the Taguchi method is to reduce the number of simulations which are required to study the effect of design variables on crash absorption indexes.

Table 4: Levels of design variables

| Parameters	Diameter (mm)	Length (mm)	Thickness (mm)
Level 1	50	100	1
Level 2	75	150	1.5
Level 3	100	200	2
Level 4	125	250	2.5
Level 5	150	300	3

3.4.2. Artificial Neural Network

Artificial Neural Network (ANN) is known as one of the most useful methods to model intricate input-output systems [61]. Design of an accurate and efficient ANN requires four steps [29, 62]:

- The suitable architecture of the ANN selection which includes the number and size of the hidden layers.

- Training parameters selection, e.g. the weight adjusting.
- Selection and preparation of the proper set of data which will be used in training and testing of the ANN.
- Defining of iteration number.

In the present study, six ANN models are fitted using three input elements, namely diameter, length and thickness which are corresponded to F_{Mean}, F_{Max}, TEA, CFE, SEA and TE as target elements, separately. **Error! Reference source not found.** illustrates the schematic of fitted ANN model.
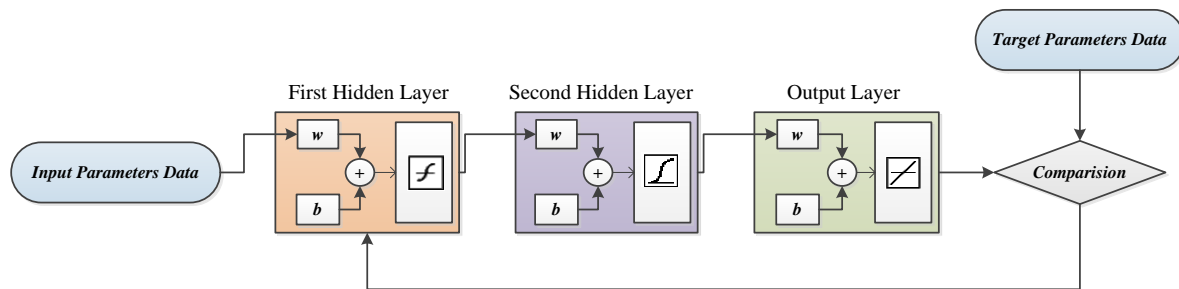
Figure 9:   Schematic of ANN fitted models.

In the present study, train, validation and test ratio are set to 0.7, 0.15 and 0.15 respectively. Furthermore, a suitable number and size of hidden layers of the mentioned models are determined by try and error as shown in Figure 9:. Accordingly, the fitted models contains two hidden layers which the first one has tangent sigmoid and the second one has a logarithmic sigmoid transfer function. Moreover, the linear transfer function is appeared to be the best choice for output layers for both models.

4. Results and Discussion

4.1. Micro-structures and Mechanical Properties

In the present study, to achieve an isotropic mechanical property of Mg-Li LZ71, the effect of different annealing temperatures on mechanical properties and microstructure of warm-rolled mentioned alloy are studied. As can be seen from Figure 10: HCP and BCC phases of LZ71 are illustrated which HCP phase is speared in BCC one without specified orientation. Moreover, Figure 11: depicts RD-ND section OM images of as rolled and annealed samples at 200^0 C and 350^0 C. From this figure, dynamic recrystallization (DRX) has accrued during the rolling process which caused fined grain production besides a considerable high level of energy in the grains boundaries as depicted in Figure 11:.a and b. Also, Figure 11:.c and d illustrate a recovery in the specimen grains which has been annealed at 200^0 C. This is obvious that the grains have not been shaped homogeneously at the mentioned heat treatment process. On the other hand, at the 350^0 C annealing temperature, the grains have grown completely homogeneous as shown in Figure 12:.e and f.
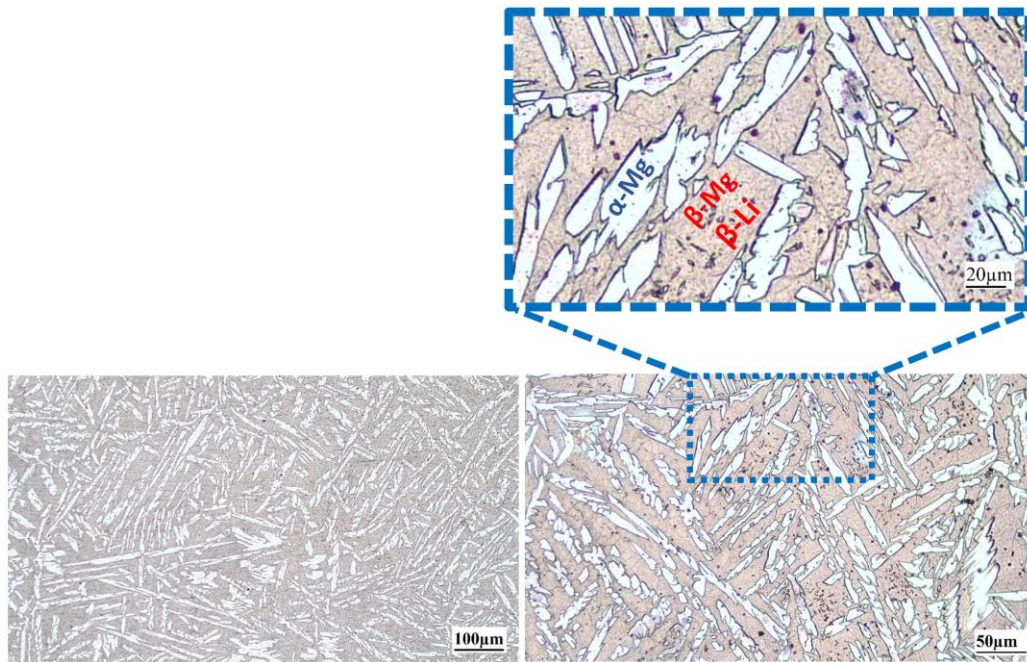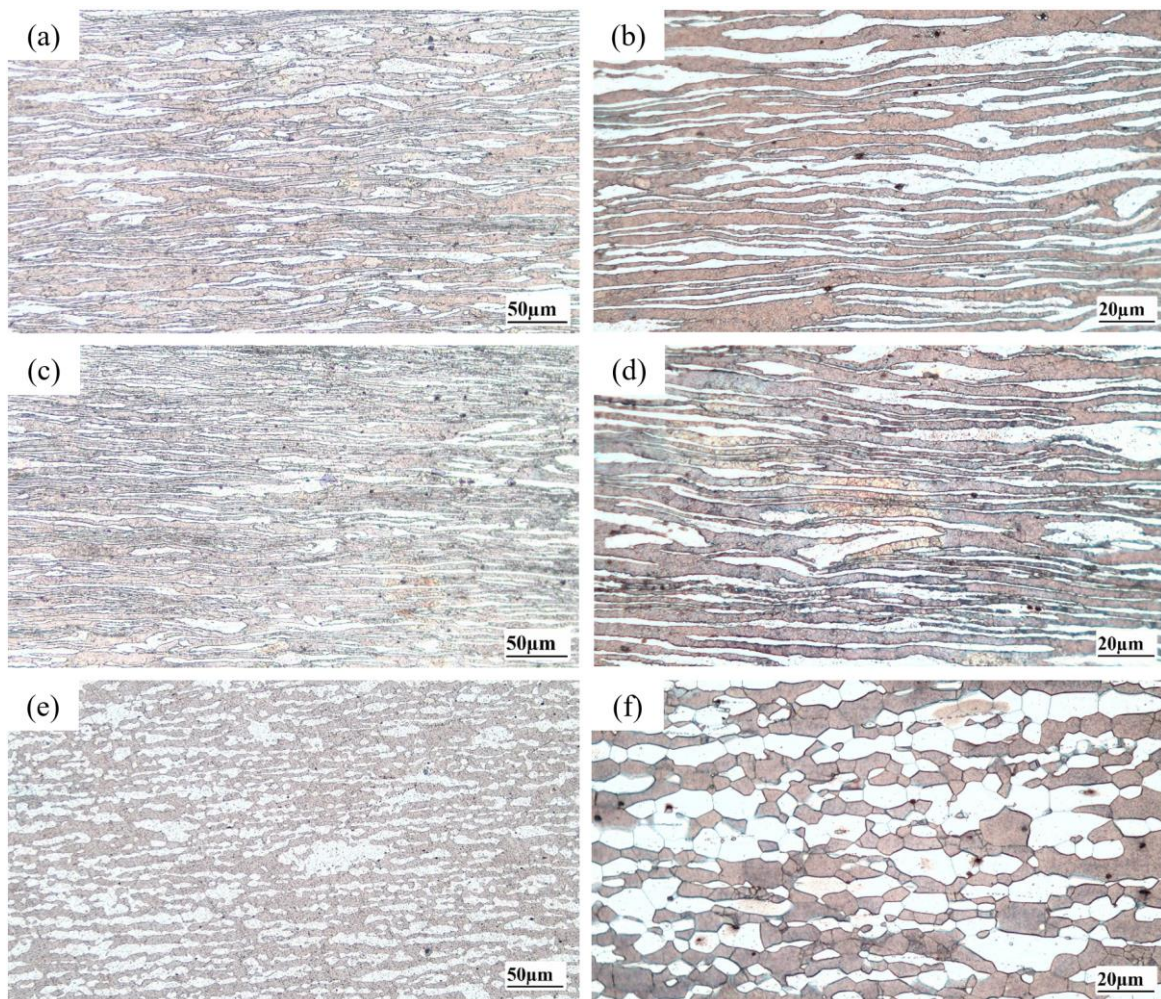
Figure 10: As cast LZ71 alloy OM images.

Figure 11: OM images of specimens: (a) and (b) as rolled, (c) and (d) annealed at 200^0 C, (e) and (f) annealed at 350^0 C.

Tensile tests results are presented in Figure 12:. Although yield and tensile strength of as rolled (Figure 12:. a) and annealed at 200^0 C (Figure 12:. b) samples are more than the samples which are annealed at 350^0 C (Figure 12:. c), mechanical properties of RD, 45^0 and TD samples which experienced 350^0 C heat treatment are considerably similar to each other. This similarity of mechanical properties shows that the plate which has been annealed at 350^0 C reached to isotropic properties.

This is concluded from the tensile tests results that the values of ultimate stress, yield stress, and elastic modulus of RD, 45^0 and TD samples are similar to each other in each heat treatment temperature but there is an obvious variation in their elongation at break point. The RD samples are shown the maximum elongation while TD sample had the minimum one. Also, the value of this parameter converges in different directions by increasing the temperature of the annealing process. On the other hand, increasing the annealing temperature causes the homogeneity of the mechanical properties of the rolled sheet in different directions. Therefore, it can be stated that the warm-rolled LZ71 sheet has become completely isotropic at the annealing temperature of 350^0 C. However, it is observed that the ultimate stress decreases by increasing the temperature.
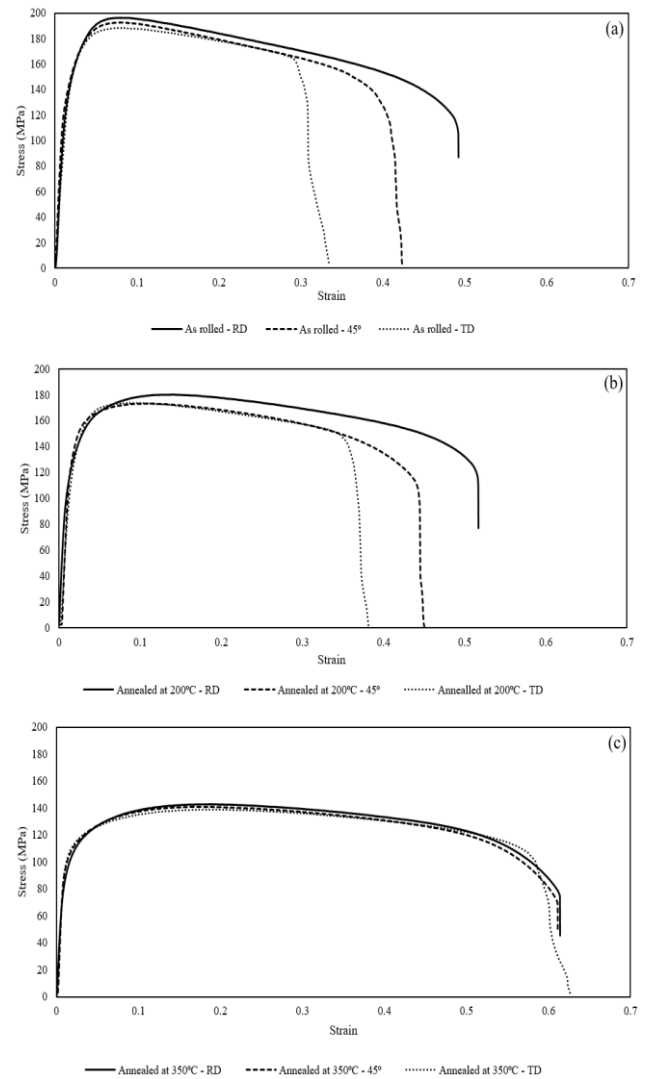
Figure 12: Stress-strain curve of RD, 45^0 and TD specimens: a) as rolled, b) 200^0 C annealing temperature, c) 350^0 C annealing temperature.
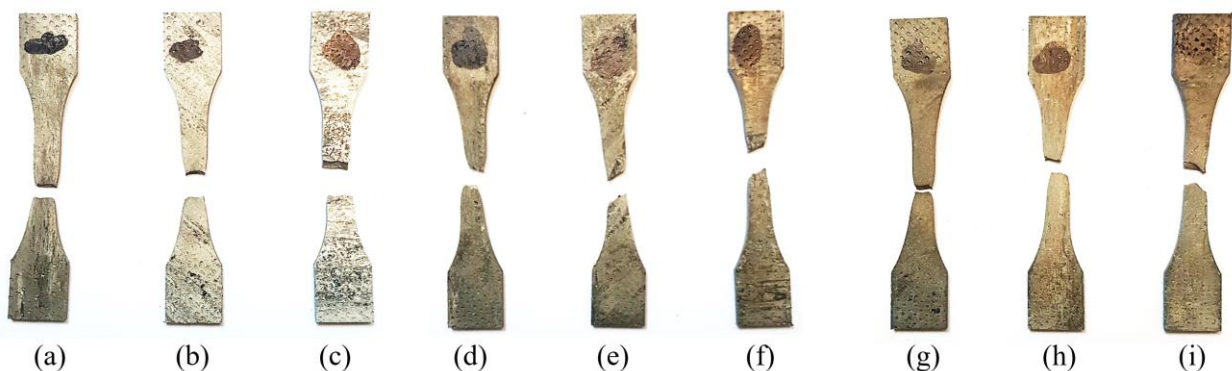
Figure 13: Tensile tests specimens: a) as rolled RD, b) as rolled 45^0 , c) as rolled TD, d) 200^0 C annealing temperature RD, e) 200^0 C annealing temperature 45^0 , f) 200^0 C annealing temperature TD, g) 350^0 C annealing temperature RD, h) 350^0 C annealing temperature 45^0 , i) 350^0 C annealing temarure TD.

In the present work stress-strain curve of warm-rolled LZ71 which has been annealed at 350^0 C, is used to simulate quasi-static crash behavior of circular tube. This is due to the isotropic

mechanical properties which are suitable for high deformation structural applications.

4.2. Energy absorption

4.2.1. Comparison of LZ71 and AA6082 in Energy Absorption Parameters

To compare the parameters of energy absorption of LZ71 and AA6082, results of tube crash simulation with A1, A2, A4, A5, and A7 dim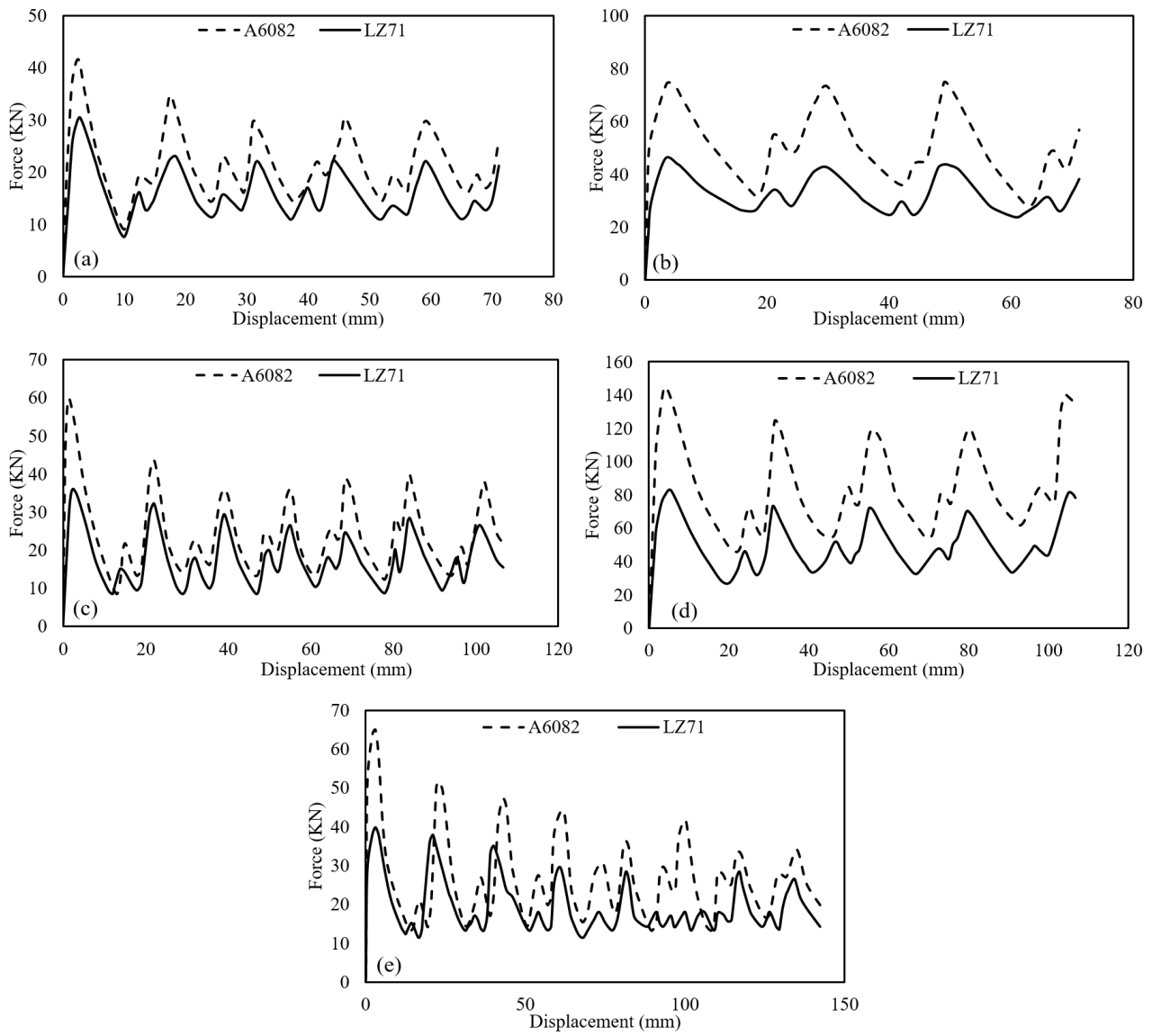ensions are studied. Crush mode of the samples are illustrated in Figure 14: which indicates A2, A4 and A5 models of LZ71 and AA6082 have been collapsed pretty similarly (Figure 14:. b, c, d). By contrast, A1 LZ71 is crushed reversely (the first fold is started from the bottom of the tube) (Figure 14:. a) and A7 LZ71 crushing mode shape is mixed of symmetric and diamond (Figure 14:. e). Figure 15: compares force-displacement curves of the models which shows mean and maximum crush force of LZ71 tubs are considerably lower than AA6082 ones.
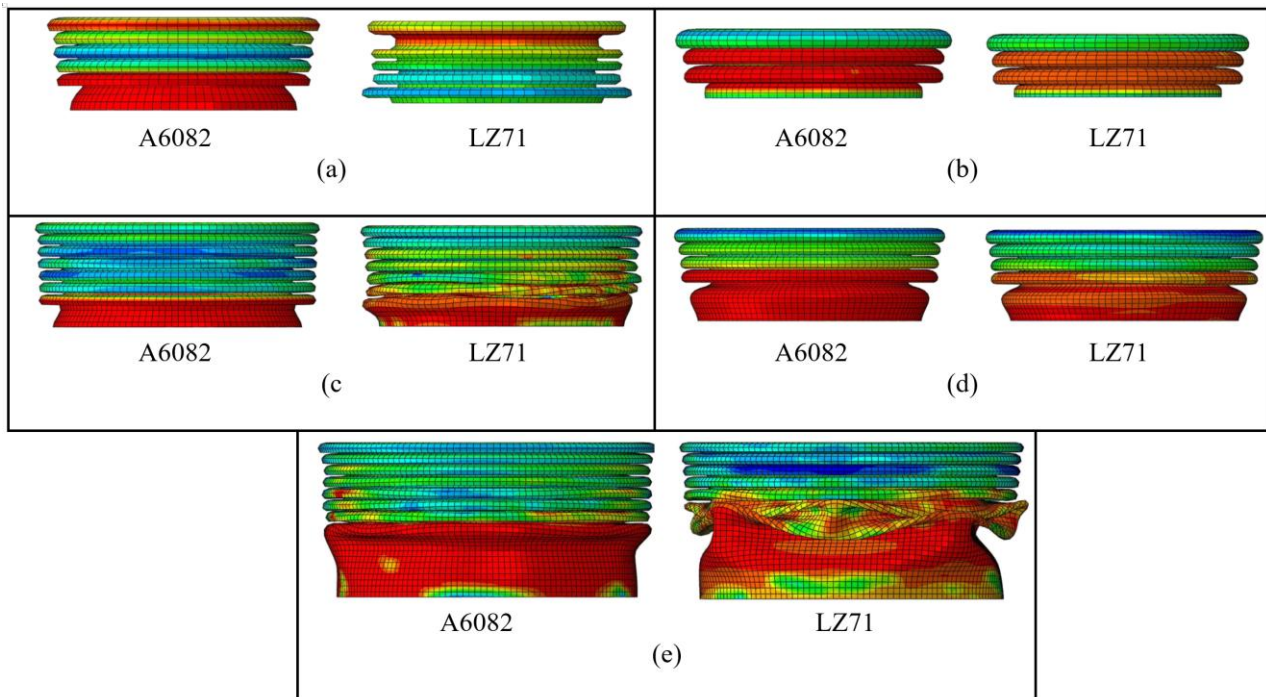
Figure 14: Crush mode comparison of LZ71 versus AA6082: a) A1, b) A2, c) A4, d) A5, e) A7.

To study more comprehensively, the crash energy absorption parameters, videlicet F_{mean}, F_{max}, TEA, CFE, and SEA are presented in Table 5:. Although F_{mean}, F_{max}, and TEA have reduced by changing the material from AA6082 to LZ71, CFE, and SEA have seen an obvious increase. F_{Mean} of A2 and A5 experienced more reduction than the other three samples by 33.648% and 36.601% respectively. Moreover, the maximum changes in F_{Max} and TEA are related to A5 sample by -42.982% and -36.601, respectively.

By changing material, both CFE and SEA have risen for all samples which amongst them CFE of A4 sample and SEA of A1 sample have increased more than others by 19.838% and 28.104% respectively. The results presented in Table 5: depicts that LZ71 alloy has obviously better crash energy absorption performance compared to AA6082.

Figure 15: Force-Displacement results of LZ71 versus AA6082: a) A1, b) A2, c) A4, d) A5 and e) A7.

Energy absorption study of warm-rolled dual-phase LZ71 magnesium alloy hollow tube using ANN

Table 5: Comparison of energy absorption parameters of LZ71 versus AA6082.

Specimen No.		A1	A2	A4	A5	A7
	AA6082 (KN)	21.450	49.008	24.149	84.310	26.725
F_{mean}	LZ71 (KN)	15.978	32.518	17.457	53.452	19.404
	Change (%)	-25.510	-33.648	-27.713	-36.601	-27.392
	AA6082 (KN)	41.650	74.360	59.850	145.360	61.130
F_{max}	LZ71 (KN)	30.511	45.858	36.102	82.881	39.904
	Change (%)	-26.744	-38.330	-39.679	-42.982	-34.723
	AA6082 (J)	1525.499	3485.458	2576.267	8994.202	3801.328
TEA	LZ71(J)	1136.350	2312.663	1862.315	5702.224	2760.060
	Change (%)	-25.510	-33.648	-27.713	-36.601	-27.392
	AA6082 (KN/KN)	0.515	0.659	0.404	0.580	0.437
CFE	LZ71 (KN/KN)	0.524	0.709	0.484	0.645	0.486
	Change (%)	1.685	7.592	19.838	11.192	11.230
	AA6082 (J/Kg)	21792.846	24896.129	16101.669	28106.880	13576.171
SEA	LZ71 (J/Kg)	27917.596	28408.508	20016.916	30644.914	16952.146
	Change (%)	28.104	14.108	24.316	9.030	24.867

4.2.2. Sensitivity of Energy Absorption Parameters of LZ71 Tubes to Dimensional Parameters

Using the Taguchi method the numbers of simulations are reduced from 125 to 25 which are shown in Table 6:. Also, results of simulations have been presented in this table. As mentioned before, to study the crushing behavior of LZ71 tubes six models are fitted. In all models dimensional parameters, namely diameter, length, and thickness were input parameters. Also for each model F_{Mean}, F_{Max}, TEA, CFE, SEA, and TE were introduced as output parameter, separately.

4.2.3. Approximation Results

According to the available inputs and outputs variable presented in Table 6: and using ANN, the fitted models between input and output data is made for tube diameter of 50 to 150 mm, a tube length of 100 to 300 mm and tube thicknesses of 1 to 3 mm. The calculated error for the ANN fitted model is under 5% which is proper for such problems. To comparison and analysis the present

case properly, surfaces of the output parameters in terms of tube length and diameter are plotted. Moreover, the surface plots of these parameters in terms of tube thickness and diameter are presented as well.

Figure 16: to **Error! Reference source not found.** illustrate the surface plots of F_{Mean}, F_{Max}, TAE CFE, SEA, and TE respectively in terms of dimensional parameters. These surface plots have been created using the correlation equations of the mentioned crash parameters in terms of the dimensional parameters, presented in equations (6) to (11). These equations have been derived using the trained ANN models.

From the Figure 16:.a, F_{Mean} approximately remains steady against the rise of the tube length and rises when the diameter increases. In the other words, the effect of diameter changes is considerable more than tube length on F_{Mean}. Figure 16:.b illustrates the growth of thickness will cause the rise of F_{Mean}. Moreover, the surface plots depict that the influence of thickness changes on the F_{Mean} is larger as compared to the effect of the specimen diameter.

Table 6: Results of selected model using Taguchi Method.

Model No.	D_m (mm)	L (mm)	t (mm)	M (Kg)	F_{Mean} (KN)	F_{Max} (KN)	δ (mm)	TEA (J)	CFE	SEA (J/Kg)	TE
1	50	100	1	0.025	8.63	15.26	70	604.39	0.57	24507.41	0.40
2	50	150	1.5	0.056	14.99	28.71	105	1574.27	0.52	28371.11	0.37
3	50	200	2	0.099	20.76	35.92	140	2906.69	0.58	29465.82	0.40
4	50	250	2.5	0.154	26.35	41.25	175	4611.01	0.64	29915.52	0.45
5	50	300	3	0.222	29.94	43.65	210	6286.97	0.69	28325.63	0.48
6	75	100	1.5	0.056	16.73	34.82	70	1171.34	0.48	21109.60	0.34
7	75	150	2	0.111	25.73	51.00	105	2702.00	0.51	24347.47	0.35
8	75	200	2.5	0.185	36.78	64.18	140	5148.75	0.57	27836.91	0.40
9	75	250	3	0.277	47.14	78.60	175	8249.35	0.60	29733.59	0.42
10	75	300	1	0.111	9.69	23.22	210	2035.82	0.42	18344.55	0.29
11	100	100	2	0.099	33.83	65.50	70	2368.41	0.52	24009.15	0.36
12	100	150	2.5	0.185	47.45	80.87	105	4982.52	0.59	26938.16	0.41
13	100	200	3	0.296	63.64	110.19	140	8909.03	0.58	30104.38	0.40
14	100	250	1	0.123	10.67	29.48	175	1866.55	0.36	15137.34	0.25
15	100	300	1.5	0.222	18.52	38.07	210	3889.70	0.49	17524.83	0.34
16	125	100	2.5	0.154	55.22	93.50	70	3865.46	0.59	25078.51	0.41
17	125	150	3	0.277	75.12	125.11	105	7887.19	0.60	28428.24	0.42
18	125	200	1	0.123	12.77	34.20	140	1787.34	0.37	14494.99	0.26
19	125	250	1.5	0.231	24.36	46.18	175	4262.22	0.53	18435.08	0.37
20	125	300	2	0.370	40.31	73.50	210	8464.64	0.55	22882.18	0.38
21	150	100	3	0.222	85.08	145.58	70	5955.22	0.58	26830.92	0.41
22	150	150	1	0.111	15.96	38.31	105	1676.06	0.42	15102.75	0.29
23	150	200	1.5	0.222	30.25	59.55	140	4234.48	0.51	19078.24	0.36
24	150	250	2	0.370	45.32	81.94	175	7931.35	0.55	21440.57	0.39
25	150	300	2.5	0.555	59.64	103.29	210	12523.91	0.58	22570.33	0.40

$$Y_1 = -15.6921 + 0.7398D + 0.0250L - 4.1666 \times 10^{-4}D^2 + 3.0703 \times 10^{-4}L^2 - 1.9110 \times 10^{-3}DL,$$

$$Y_2 = 11.6469 - 0.1031D - 11.3395t - 4.1666e\text{-}4D^2 + 3.1456t^2 + 0.2303Dt,$$

$$Y_3 = 4.8663 - 0.4244Y_1 + 1.1128Y_2 + 7.4117 \times 10^{-3}Y_1^2 - 1.9467 \times 10^{-5}Y_2^2 - 2.9323 \times 10^{-3}Y_1Y_2,$$

$$Y_4 = -7.6953 + 1.0307Y_2 + 0.0999L - 1.3751 \times 10^{-5}Y_2^2 - 2.7146 \times 10^{-4}L^2 - 1.6358 \times 10^{-4}Y_2L,$$

$$F_{Mean} = -0.0909 + 0.9823Y_3 + 0.0325Y_4 - 0.1083Y_3^2 - 0.0884Y_4^2 + 0.1966Y_3Y_4 \tag{6}$$

$$Y_1 = 11.5210 + 0.1631D - 19.8513t - 1.9573 \times 10^{-3}D^2 + 4.6346t^2 + 0.3736Dt,$$

$$Y_2 = -14.5533 + 0.2172L + 0.9486Y_{13} - 6.0040 \times 10^{-4}L^2 + 4.5021e\text{-}4Y_{13}^2 - 7.407 \times 10^{-5}LY_{13},$$

$$F_{Max} = -2.6563 + 0.8334Y_2 + 7.6418t - 9.8598 \times 10^{-4}Y_2^2 - 3.3611t^2 + 0.1245Y_2t \tag{7}$$

$$Y_1 = -3957.7395 - 0.7663D + 3989.3844t + 0.1601D^2 - 256.8008t^2 + 0.2321Dt,$$

$$Y_2 = -4673.6945 + 8.8352L + 3631.3678t + 0.0150L^2 - 256.8008t^2 + 1.9061Lt,$$

$$Y_3 = 987.6594 - 13.5478D + 6.0246L + 0.1601D^2 + 0.0150L^2 + 0.0662DL,$$

$$Y_4 = 1.5478 \times 10^{-4} + 0.2004Y_1 + 0.5386Y_2 - 1.8371 \times 10^{-4}Y_1^2 - 2.1368 \times 10^{-4}Y_2^2 + 4.6461 \times 10^{-4}Y_1Y_2,$$

$$TEA = -5.2499 \times 10^{-5} + 0.4657Y_3 + 0.0643Y_4 + 4.3528 \times 10^{-5}Y_3^2 + 4.2644 \times 10^{-5}Y_4^2 - 4.5007 \times 10^{-6}Y_3Y_4 \tag{8}$$

$$Y_1 = 0.7629 - 4.0679 \times 10^{-3}D - 3.8170L + 2.2548 \times 10^{-5}D^2 + 2.1501 \times 10^{-6}L^2 - 4.7593 \times 10^{-6}DL,$$

$$Y_2 = 0.5215 - 5.2701 \times 10^{-3}D + 0.1987t + 2.2548 \times 10^{-5}D^2 - 0.0301t^2 + 1.2516 \times 10^{-4}Dt,$$

$$Y_3 = 4.0927 - 20.5623Y_1 + 6.6029Y_2 + 21.1610Y_1^2 - 3.3644Y_2^2 - 4.1391Y_1Y_2,$$

$$CFE = 0.3857 + 5.9301Y_3 - 6.3671Y_2 + 8.9837Y_3^2 + 19.0443Y_2^2 - 26.7242Y_3Y_2 \tag{9}$$

$$Y_1 = 28375.5445 - 282.7104D + 6708.8609t + 0.7565D^2 - 1093.0900t^2 + 32.4318Dt,$$

$$Y_2 = 15428.7905 - 11.6388L + 6092.9677t - 0.0997L^2 - 1093.0900t^2 + 19.2954Lt,$$

$$Y_3 = 30054.4174 - 158.6945D + 56.5281L + 0.7565D^2 - 0.0997L^2 - 0.2958DL,$$

$$Y_4 = 2.9896 \times 10^{-5} + 1.0064Y_1 - 0.1628Y_2 + 5.7990 \times 10^{-5}Y_1^2 + 7.1886 \times 10^{-5}Y_2^2 - 1.2413 \times 10^{-4}Y_1Y_2,$$

$$Y_5 = 5.5811 \times 10^{-5} + 6.5598 \times 10^{-5}t + 0.6584Y_3 + 6.1451 \times 10^{-5}t^2 - 3.4550 \times 10^{-6}Y_3^2 + 0.2110tY_3,$$

$$SEA = -1.0300 \times 10^{-4} - 2.8158Y_4 + 3.7292Y_5 - 1.2734 \times 10^{-4}Y_4^2 - 3.2507 \times 10^{-4}Y_5^2 + 4.5660 \times 10^{-4}Y_4Y_5 \tag{10}$$

$$Y_1 = 0.3650 - 3.6891 \times 10^{-3}D + 0.1391t + 1.5784 \times 10^{-5}D^2 - 0.0211t^2 + 8.7612 \times 10^{-5}Dt,$$

$$Y_2 = 0.5340 - 2.8475 \times 10^{-3}D - 2.6719 \times 10^{-4}L + 1.5784 \times 10^{-5}D^2 + 1.5051 \times 10^{-6}L^2 - 3.3315 \times 10^{-6}DL,$$

$$Y_3 = 2.8649 + 6.6029Y_1 - 20.5623Y_2 - 4.8062Y_1^2 + 30.2301Y_2^2 - 5.9130Y_1Y_2,$$

$$Y_4 = 0.3650 - 3.6891 \times 10^{-3}D + 0.1391t + 1.5784 \times 10^{-5}D^2 - 0.0211t^2 + 8.7612 \times 10^{-5}Dt,$$

$$TE = 0.2700 + 5.9301Y_3 - 6.3671Y_4 + 12.8334Y_3^2 + 27.2061Y_4^2 - 38.1775Y_3Y_4 \tag{11}$$
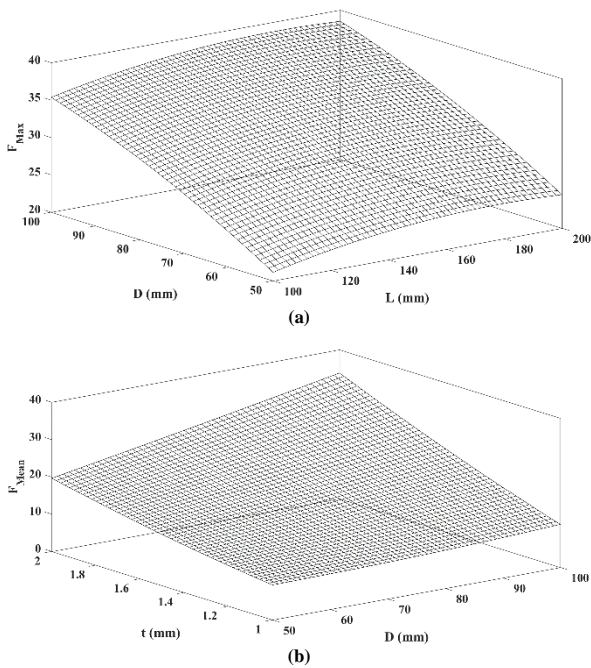
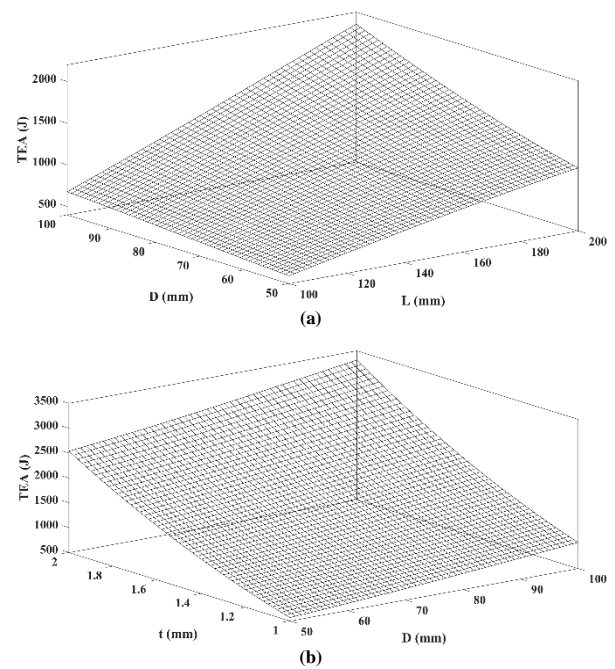**Figure 16:** Surface plot of F_{mean} as a function of: a) L and D, b) D and t.

Figure 17:.a shows that F_{Max} increases considerably against the growth of diameter while the gain of the length make it experience a mild increase. From Figure 17:.b F_{Max} has risen obviously due to the increase of thickness and also the effect of thickness changes on the F_{Max} is almost more than that of the diameter.
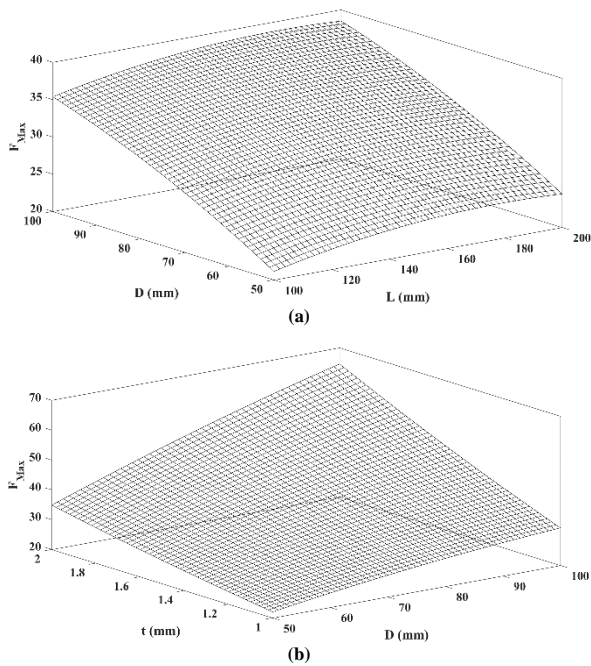
Figure 17: Surface plot of F_{max} as a function of: a) L and D, b) D and t.

TEA experienced a mild increase against rise of diameter while the effect of length changes had considerable effect (Figure 18:.a). Also similar to

F_{Mean}, the influence of thickness value is obviously more than that of diameter (Figure 18:.b).

Figure 18: Surface plot of TEA as a function of: a) L and D, b) D and t.

As can be seen from Figure 19: to Figure 21:, CFE, SEA, and TE have been influenced slightly by conversions of the length of specimens while the effects of changes of model thickness and diameter are considerable on the mentioned parameters.
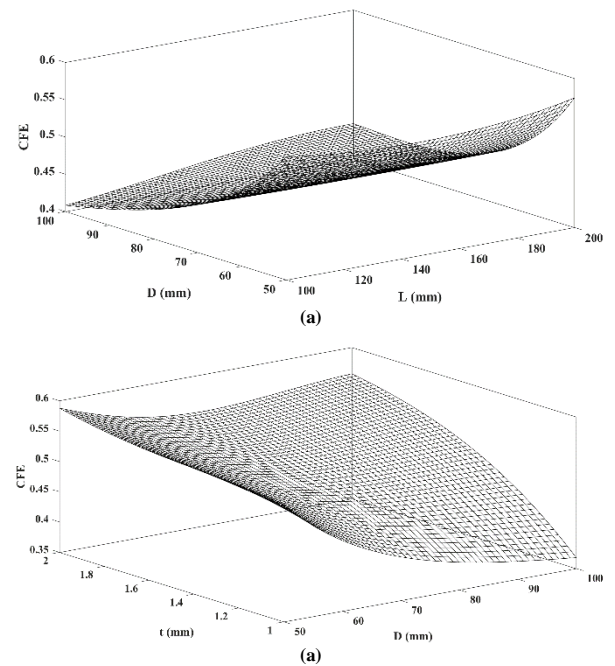
Figure 19: Surface plot of CFE as a function of: a) L and D, b) D and t.
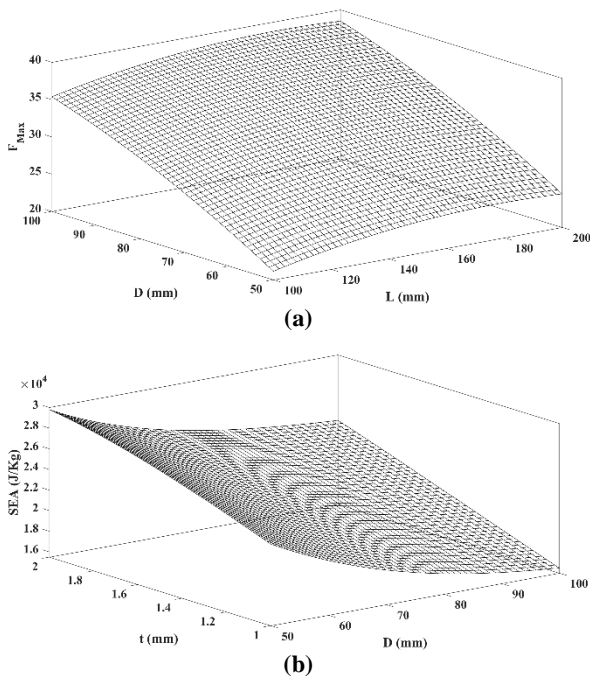
Figure 20: Surface plot of SEA as a function of: a) L and D, b) D and t.
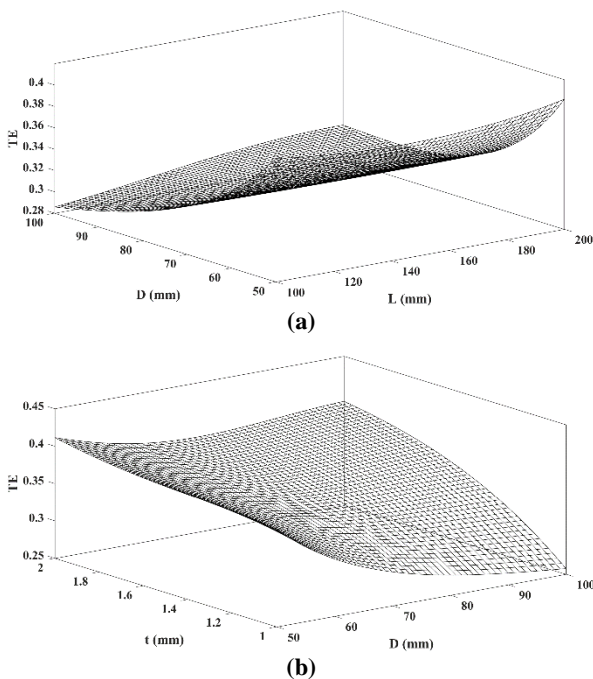

Figure 21: Surface plot of TE as a function of: a) L and D, b) D and t.

5. Conclusion

In this paper, crashworthiness of LZ71 magnesium alloy hollow tube has been surveyed numerically. To achieve mechanical properties of LZ71 sheet, the uniaxial tensile test has been applied to drive stress-strain curves. Since isotropic materials show proper crushing behavior in high deformation situations, rolled specimen annealed at 200^0 C and 350^0 C.

- Isotropic mechanical behavior has observed in specimens which had annealed at 350^0 C. Therefore, results of tensile tests of the samples annealed at 350^0 C is used to simulate crush behavior of LZ71 hollow tube.
- FE models have been validated by the experimental results of aluminum AA6082 tube crash which showed excellent performances regarding the crush mode shape and force-displacement graphs.
- The crash energy absorption parameters including peak crush force (F_{Max}), mean crush force (F_{Mean}), total energy absorption (TAE), crush force efficiency (CFE), specific energy absorption (SEA) and total efficiency (TE), are compared between experiments and simulations which indicate that the simulations results were completely close to the experimental outcomes.
- The energy absorption performance of LZ71 and AA6082 have been compared to each other which concluded that LZ71 crashworthiness characterizations are much better than AA6082 particularly in thinner samples that this is due to LZ71 extremely low density.
- The sensitivity of energy absorption parameters of LZ71 has been studied with the help of Taguchi method (to select dimensional parameters of simulation models) and Artificial Neural Network (to fit the approximation model).
- The results of sensitivity analysis illustrate that the influences of thickness variations on F_{Mean}, and TEA are much more considerable with compared to length and diameter.
- The influences of the model length changes on the CFE, SEA, and TE were obviously lower than that of the thickness and diameter.

References

[1] R. Szlosarek, F. Bombis, M. Mühler, M. Kröger, and T. Karall, "Development of carbon fibre-reinforced plastic (CFRP) crash absorbers with stable crushing behaviour considering the connection to the bumper system," *Materialwissenschaft und Werkstofftechnik,* vol. 47, pp. 1099-1108, 2016.

[2] O. M. Qureshi, E. Bertocchi, Z. Qaiser, and K. A. Awan, "Frequency embedded box beam crash absorbers under oblique impacts," *Thin-Walled Structures,* vol. 75, pp. 1-7, 2014.

[3] Z. Qaiser, O. M. Qureshi, S. Johnson, and A. A. Khan, "Thin walled circular beams with sinusoidal embedded patterns under axial impacts," *Thin-Walled Structures,* vol. 99, pp. 76-82, 2016.

[4] D. Delsart, G. Portemont, and M. Waimer, "Crash testing of a CFRP commercial aircraft sub-cargo fuselage section," *Procedia Structural Integrity,* vol. 2, pp. 2198-2205, 2016.

[5] H. Zarei, "Experimental and numerical crashworthiness investigation of hybrid composite aluminum tubes under dynamic axial and oblique loadings," 2015.

[6] C. Bedon, M. Arrigoni, F. Santos, and L. Figuli, "Advancements in Design and Analysis of Protective Structures," *Advances in Civil Engineering,* vol. 2018, 2018.

[7] M. Altin, S. Halis, and H. S. Yücesu, "Investigation of the Effect of Corrugated Structure on Crashing Performance in Thin-Walled Circular Tubes," *International Journal of Automotive Science and Technology,* vol. 1, pp. 1-7, 2017.

[8] S. Muhammad Nasiruddin, A. Hambali, J. Rosidah, W. Widodo, and M. Ahmad, "A Review of Energy Absorption of Automotive Bumper Beam," *International Journal of Applied Engineering Research,* vol. 12, pp. 238-245, 2017.

[9] E. Demirci and A. R. Yıldız, "An experimental and numerical investigation of the effects of geometry and spot welds on the crashworthiness of vehicle thin-walled structures," *Materials Testing,* vol. 60, pp. 553-561, 2018.

[10] J. D. Littell, K. E. Jackson, M. S. Annett, M. D. Seal, and E. L. Fasanella, "The development of two composite energy absorbers for use in a transport rotorcraft airframe crash testbed% 28tract 2% 29 full-scale crash test," in *71st AHS International Annual Forum and Technology Display*; 5-7 May 2015; Virginia Beach, VA; United States.

[11] C. G. Martin and A. Arokkiaswamy, "Design and development of energy absorption fixtures for safe belly landing on land for a typical aircraft configuration," *International Journal of Advanced Scientific Research and Management*, Vol. 1 Issue 2, pp. 54-60, 2016.

[12] J. Marzbanrad and M. R. Ebrahimi, "Multi-Objective Optimization of aluminum hollow tubes for vehicle crash energy absorption using a genetic algorithm and neural networks," *Thin-Walled Structures,* vol. 49, pp. 1605-1615, 2011.

[13] J. Marzbanrad and A. Keshavarzi, "A numerical and experimental study on the crash behavior of the extruded aluminum crash box with elastic support," *Latin American Journal of Solids and Structures,* vol. 11, pp. 1329-1348, 2014.

[14] P. Khalili, F. Tarlochan, A. Hamouda, and K. Al-Khalifa, "Energy absorption capability of thin-walled aluminium tubes under crash loading," *Journal of Mechanical Engineering and Sciences*, Volume 9, pp. 1734-1743 2015.

[15] N. Ahmed, P. Xue, and N. Zafar, "Dynamic axial crushing of bitubular tubes with curvy polygonal inner-tube sections," *International Journal of Computational Materials Science and Engineering,* vol. 6, p. 1750024, 2017.

[16] M. D. Goel, "Deformation, energy absorption and crushing behavior of single-, double-and multi-wall foam filled square and circular tubes," *Thin-Walled Structures,* vol. 90, pp. 1-11, 2015.

[17] X. Zhang and G. Cheng, "A comparative study of energy absorption characteristics of foam-filled and multi-cell square columns," *International Journal of Impact Engineering,* vol. 34, pp. 1739-1752, 2007.

[18] A. Mahmoodi, M. H. Shojaeefard, and H. Saeidi Googarchin, "Theoretical development and numerical investigation on energy absorption behavior of tapered multi-cell tubes," *Thin-Walled Structures,* vol. 102, pp. 98-110, 2016.

[19] S. Yao, Y. Xing, and K. Zhao, "Crashworthiness analysis and multiobjective optimization for circular tubes with functionally graded thickness under multiple loading angles," *Advances in Mechanical Engineering,* vol. 9, pp. 1-11, 2017.

[20] A. Niknejad and D. M. Rahmani, "Experimental and theoretical study of the lateral compression process on the empty and foam-filled hexagonal columns," *Materials & Design,* vol. 53, pp. 250-261, 2014.

[21] A. Baroutaji, M. D. Gilchrist, D. Smyth, and A. G. Olabi, "Analysis and optimization of sandwich tubes energy absorbers under lateral loading," *International Journal of Impact Engineering,* vol. 82, pp. 74-88, 2015.

[22] A. Niknejad and M. Moeinifard, "Theoretical and experimental studies of the external inversion process in the circular metal tubes," *Materials & Design,* vol. 40, pp. 324-330, 2012.

[23] X. M. Qiu, L. H. He, J. Gu, and X. H. Yu, "An improved theoretical model of a metal tube under free external inversion," *Thin-Walled Structures,* vol. 80, pp. 32-37, 2014.

[24] K. C. Shin, J. J. Lee, K. H. Kim, M. C. Song, and J. S. Huh, "Axial crush and bending collapse of an aluminum/GFRP hybrid square tube and its energy absorption capability," *Composite Structures,* vol. 57, pp. 279-287, 2002.

[25] G. Sun, X. Tian, J. Fang, F. Xu, G. Li, and X. Huang, "Dynamical bending analysis and optimization design for functionally graded thickness (FGT) tube," *International Journal of Impact Engineering,* vol. 78, pp. 128-137, 2015.

[26] R. Sturm and F. Heieck, "Energy absorption capacity of braided frames under bending loads," *Composite Structures,* vol. 134, pp. 957-965, 2015.

[27] B. Mashadi, J. Marzbanrad, and A. Afkar, "Blade shape and thickness influence of multi-blade cutting tool during axial impact to the extruded aluminum tube," *Mechanics,* vol. 22, pp. 229-236, 2016.

[28] J. Marzbanrad, B. Mashadi, A. Afkar, and S. Mahdavi, "A Comparison between cutting and folding modes of an extruded aluminum alloy tube during impact using ductile failure criterion," *Mechanics & Industry,* vol. 17, pp. 208.1-208.15, 2016.

[29] J. Marzbanrad, B. Mashadi, A. Afkar, and M. Pahlavani, "Dynamic rupture and crushing of an extruded tube using artificial neural network (ANN) approximation method," *Journal of Central South University,* vol. 23, pp. 869-879, 2016.

[30] A. Niknejad, B. Rezaei, and G. H. Liaghat, "Empty circular metal tubes in the splitting process–theoretical and experimental studies," *Thin-Walled Structures,* vol. 72, pp. 48-60, 2013.

[31] A. A. Nia and H. Khodabakhsh, "The effect of radial distance of concentric thin-walled tubes on their energy absorption capability under axial dynamic and quasi-static loading," *Thin-Walled Structures,* vol. 93, pp. 188-197, 2015.

[32] S. H. Lee, H. Y. Kim, and S. I. Oh, "Cylindrical tube optimization using response surface method based on stochastic process," *Journal of Materials Processing Technology,* vol. 130–131, pp. 490-496, 2002.

[33] S. Hosseinipour and G. Daneshi, "Experimental studies on thin-walled grooved tubes under axial compression," *Experimental mechanics,* vol. 44, pp. 101-108, 2004.

[34] K. Yamazaki and J. Han, "Maximization of the crushing energy absorption of cylindrical shells," *Advances in Engineering Software,* vol. 31, pp. 425-434, 2000.

[35] E. Acar, M. Guler, B. Gerceker, M. Cerit, and B. Bayram, "Multi-objective crashworthiness optimization of tapered thin-walled tubes with axisymmetric indentations," *Thin-Walled Structures,* vol. 49, pp. 94-105, 2011.

[36] G. Nagel and D. Thambiratnam, "Computer simulation and energy absorption of tapered thin-walled rectangular tubes," *Thin-Walled Structures,* vol. 43, pp. 1225-1242, 2005.

[37] S. Hou, X. Han, G. Sun, S. Long, W. Li, X. Yang, and Q. Li, "Multiobjective optimization for tapered circular tubes," *Thin-Walled Structures,* vol. 49, pp. 855-863, 2011.

[38] A. Taştan, E. Acar, M. A. Güler, and Ü. Kılınçkaya, "Optimum crashworthiness design of tapered thin-walled tubes with lateral circular cutouts," *Thin-Walled Structures,* vol. 107, pp. 543-553, 2016.

[39] D. Rahmatabadi, R. Hashemi, B. Mohammadi, and T. Shojaee, "Experimental evaluation of the plane stress fracture toughness for ultra-fine grained aluminum specimens prepared by accumulative roll bonding process," *Materials Science and Engineering: A,* vol. 708, pp. 301-310, 2017.

[40] D. Rahmatabadi and R. Hashemi, "Experimental investigation of formability of aluminum sheets produced by cold roll bonding process used by Nakazima test," *Modares Mechanical Engineering,* vol. 17, pp. 451-454, 2017.

[41] D. Rahmatabadi, B. Mohammadi, R. Hashemi, and T. S. Shojaee, "An experimental survey of fracture toughness for nano/ultra-fine grained Al5052/Cu multi-layered composite processed by the accumulative roll bonding," *Journal of Manufacturing Science and Engineering,* 2018.

[42] D. Rahmatabadi, M. Tayyebi, A. Sheikhi, and R. Hashemi, "Fracture toughness investigation of Al1050/Cu/MgAZ31ZB multi-layered composite produced by accumulative roll bonding process," *Materials Science and Engineering: A,* vol. 734, pp. 427-436, 2018.

[43] E. Demirci and A. Yildiz, "Lightweight design of vehicle energy absorbers using steel, aluminum and magnesium alloys," in *International Conference on Engineering and Natural Sciences,* Sarajevo, 2016, pp. 1684-1691.

[44] M. Bechtold, K. Drechsler, F. Maidl, B. Moeltgen, and F. Strachauer, "Fiber composite crash structure," ed: Google Patents, 2004.

[45] A. A. Luo, E. A. Nyberg, K. Sadayappan, and W. Shi, "Magnesium front end research and development: a Canada-China-USA collaboration," in *Essential Readings in Magnesium Technology*, ed: Springer, 2016, pp. 41-48.

[46] T. Abbott, M. Easton, and R. Schmidt, "Magnesium for crashworthy components," in *Essential Readings in Magnesium Technology*, ed: Springer, 2016, pp. 463-466.

[47] M. K. Kulekci, "Magnesium and its alloys applications in automotive industry," *The International Journal of Advanced Manufacturing Technology,* vol. 39, pp. 851-865, 2008.

[48] B. L. Mordike and T. Ebert, "Magnesium: Properties, applications, potential," *Materials Science and Engineering: A,* vol. 302, pp. 37-45, 2001.

[49] K. Sahoo and P. Poddar, "Studies on magnesium alloys-properties and potential for automotive and

aerospace applications," in *Transaction of 65th Indian foundry Congress 2017*, 2017, pp. 151-156.

[50] W. Tao, Z. Milin, N. Zhongyi, and L. Bin, "Influence of rare earth elements on microstructure and mechanical properties of Mg-Li alloys," *Journal of Rare Earths,* vol. 24, pp. 797-800, 2006.

[51] Y. Tang, Q. Le, R. D. K. Misra, G. Su, and J. Cui, "Influence of extruding temperature and heat treatment process on microstructure and mechanical properties of three structures containing Mg-Li alloy bars," *Materials Science and Engineering: A,* vol. 712, pp. 266-280, 2018.

[52] M. C. Lin, S. Q. Lin, and J. Y. Uan, "Effect of annealing temperature on the microstructure and mechanical properties of an as-rolled Mg-9wt.% Li-3wt.% Al-1wt.% Zn alloy sheet," *Frontiers of Materials Science,* vol. 8, pp. 271-280, 2014.

[53] R. Pandey, S. Tekumalla, and M. Gupta, "Effect of defects on electromagnetic interference shielding effectiveness of magnesium," *Journal of Materials Science: Materials in Electronics,* pp. 1-12, 2018.

[54] M. Kiani, I. Gandikota, M. Rais-Rohani, and K. Motoyama, "Design of lightweight magnesium car body structure under crash and vibration constraints," *Journal of Magnesium and Alloys,* vol. 2, pp. 99-108, 2014.

[55] T. Wang, M. Zhang, and R. Wu, "Microstructure and properties of Mg–8Li–1Al–1Ce alloy," *Materials Letters,* vol. 62, pp. 1846-1848, 2008.

[56] X. Meng, R. Wu, M. Zhang, L. Wu, and C. Cui, "Microstructures and properties of superlight Mg–Li–Al–Zn wrought alloys," *Journal of Alloys and Compounds,* vol. 486, pp. 722-725, 2009.

[57] S. Y. Jin and W. Altenhof, "Comparison of the load/displacement and energy absorption performance of round and square AA6061-T6 extrusions under a cutting deformation mode," *International Journal of Crashworthiness,* vol. 12, pp. 265-278, 2007.

[58] S. Lu, "Impact energy absorption analysis of different thin-walled tubes with and without reinforcement," Doctor of Philosophy, School of Mechanical, Aerospace and Civil Engineering, University of Manchester, 2014.

[59] T. Mori, "The new experimental design: Taguchi's approach to quality engineering," *Amer Supplier Institude*, ISBN-13: 9780941243131,1991.

[60] D. C. Montgomery, "Design and analysis of experiments," *John wiley & sons*, ISBN-13: 9781118146927, 2017.

[61] H. Demuth, M. Beale, and M. Hagan, "Neural network toolbox TM 6 user's guide matlab," *The MathWorks2009,* 2013.

[62] T. Omar, A. Eskandarian, and N. Bedewi, "Vehicle crash modeling using recurrent neural networks," *Mathematical and Computer Modelling,* vol. 28, pp. 31-42, 1998.